A study of EWOD-driven droplets by PIV investigation

Hsiang-Wei Lu,*[a] Frederic Bottausci,[b] Jesse D. Fowler,[a] Andrea L. Bertozzi,[c] Carl Meinhart[b] and Chang-Jin "CJ" Kim[a]

Received 6th November 2007, Accepted 14th December 2007
First published as an Advance Article on the web 17th January 2008
DOI: 10.1039/b717141b

Despite the recent interest in droplet-based microfluidics using electrowetting-on-dielectric (EWOD), fundamental understanding of the fluid dynamics remains limited to two-dimensional (2D) reduction of the Navier–Stokes equation. Experimental data are in dire need to verify the predictions and advance the field. We report an investigation of the flow inside droplets actuated by EWOD *in air* using micro particle image velocimetry (μ-PIV). Using the continuity equation, we reconstruct the 3D velocity field from the 2D PIV experimental data. We present some fundamental findings and build valuable insights that will help design sophisticated EWOD microfluidic devices. For example, the results confirm that efficient mixing in a droplet may be achieved by moving the droplet along an irreversible pattern that breaks the symmetry of the two circulating inner flows.

Introduction

Due to the simple chip fabrication, ease of electronic control and low power consumption, electrowetting-on-dielectric (EWOD) has become a popular mechanism for microfluidic actuations, especially digital (droplet based) microfluidics.[1–3] The theory of electrowetting and its initial applications are well reviewed by Mugele *et al*.,[4] Fair,[5] and Moon *et al.*[6] Despite the popularity, fundamental understanding of the fluid dynamics in the drops actuated by EWOD remains limited. The available flow simulations (including commercial codes) are all based on a two-dimensional (2D) reduction of the Navier–Stokes equations, assuming a fully developed parabolic flow profile in a thin flat droplet.[7,8] It is well known that the flow in a thin and flat 2D droplet is, to the leading order, irrotational.[9] Therefore, it is necessary to understand the fluid dynamics in a thick, 3D droplet in order to design sophisticated EWOD devices for mixing.

Many studies have proposed active[10–12] and passive methods[13–15] to generate mixing for continuous liquid flows in microchannels where the flow is under a well-layered laminar condition. Although droplet-based microfluidics is not continuous (*e.g.*, a train of discrete droplets merging) and thus not expected to hold the same degree of difficulty in mixing that continuous microfluidics suffers from, the flow field within the droplets needs to be understood to evaluate the mixing. Single-plate EWOD devices have demonstrated effective mixing by oscillating the liquid–air interface of sessile drops.[16,17] For droplets confined between two parallel plates, mixing by different movement patterns has been studied for aqueous drops exposed to air[18] or surrounded by silicone oil.[19] We expect a fundamentally different flow pattern between a droplet in air and a droplet in oil, due to the significant viscosity difference of the external fluid. In addition, dye-based flow visualization in air must be considered with great care because the fluorescent dye creates a surface tension gradient, inducing a surface flow.

As a first step toward understanding the flow in a 3D droplet actuated by EWOD, we utilize micro particle image velocimetry (μ-PIV)[20,21] to characterize the microfluidic flow inside of a thick droplet with $b/R \sim 1$, where b is the separation height between the parallel plates of the EWOD device and R is the disc radius of the droplet squeezed between the plates. The droplet is uniformly seeded with 2 μm polystyrene beads, thus free of any surface tension gradient. We imaged the horizontal velocity fields on 7 planes of different heights from the bottom substrate. Using the continuity equation, we reconstruct the 3D velocity field from the 2D PIV experimental data. We present some fundamental findings and build valuable insights that will help the design of sophisticated devices and strategies for EWOD microfluidics. It is shown, for example, that a simple forward-and-back actuation strategy is inefficient for mixing purposes.

Experimental

The parallel-plate EWOD devices were developed in the University of California, Los Angeles (UCLA) Micro and Nano Manufacturing Laboratory using the Nanoelectronics Research Facility (Nanolab). Square shaped electrodes, each having 600 μm × 600 μm of area, are patterned on indium-tin oxide (ITO) coated glass wafers, which serves as the bottom substrates of the parallel-plate EWOD devices. A 500 nm blanket layer of silicon oxide is deposited by plasma enhanced chemical vapor deposition (PECVD). A final coating of Cytop® fluoropolymer (Asahi Glass, Japan) is deposited by spin coating a 6% solvated solution on the wafer with tapes covering the contact pads. Two hours of annealing at 210 °C removes the solvent, leaving

[a]*Department of Mechanical and Aerospace Engineering, UCLA, 420 Westwood Plaza, 37-129 Engineering IV Bldg., Los Angeles, CA, USA. E-mail: hwlu@ucla.edu; Tel: +1-310-825-3977*
[b]*Department of Mechanical Engineering, UCSB, Santa Barbara, CA, USA*
[c]*Department of Mathematics, UCLA, 520 Portola Plaza, Math Sciences Building, 7619D, Los Angeles, CA, USA*

a polymer layer of approximately 240 nm in thickness. The top substrate of the electrowetting device is a cleaved ITO glass wafer. Spin coating a 3% solvated solution followed by annealing gives a very thin Cytop® layer (~50 nm) on the top substrate. All fluoropolymer layers are applied and annealed just before the experiments to ensure quality of the coating. The electrowetting device is completed by a pressure-contact packaging.[22]

The experiment was conducted in the University of California, Santa Barbara (UCSB) Microfluidics Laboratory, where the μ-PIV equipment is located. The setup is illustrated in Fig. 1. The fluid used is deionized water seeded with Nile red colored fluorescent polystyrene microbeads of 2 μm in diameter (Invitrogen) at 0.01% solid concentration. The resulting particle density is 2×10^7 particles ml^{-1}. The user controls the applied potential on each electrode through a digital I/O board (Daqpad-6507, National Instrument) that controls electronic relays that pass the high voltage and the ground potential to the electrodes from the voltage source. The digital I/O board also sends a 5 V falling edge as the synchronization signal to the computer controlling the μ-PIV setup. The pulses of two frequency-doubled Nd:YAG lasers emitting green light ($\lambda = 523$ nm) are combined, directed through an optical fiber into a Nikon TE200 inverted microscope. The pulses are reflected by a long-pass filter cube onto the EWOD device and excite the fluorescent microbeads. The fluorescent emission is filtered by the long-pass filter cube and captured by a cooled 1030 × 1300 × 12 bits interline transfer CCD camera through a NA = 0.45, 10× objective lens, resulting in approximately 25 μm of depth of field.

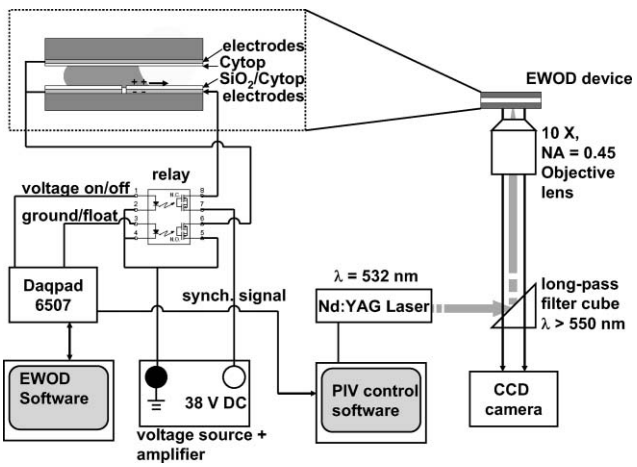

Fig. 1 EWOD device and PIV experimental setups.

Procedure

During the experiment, 0.1 μl of the seeded fluid is deposited in the device, along with 6 larger droplets of deionized water, each with 5 μl in volume. An adhesive well made of SecureSeal (Grace BioLab) seals the device with the drops in it and maintains a substrate separation of approximately 388 μm. The moisture from the large water droplets saturates the moisture level in the device to prevent evaporation of the seeded droplet. The seeded droplet is constrained by the top and the bottom substrates and has a disc diameter of approximately 800 μm. The experiment repeatedly actuates the droplet back and forth between two electrodes as illustrated in Fig. 2.

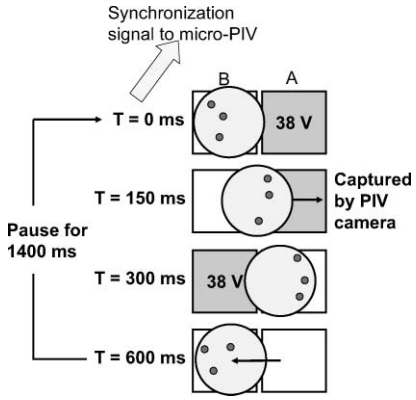

Fig. 2 One cycle of actuation sequence of the electrowetting device.

The droplet initially sits on top of electrode B. At time $t = 0$, a 38 volt DC potential is applied to electrode A, with electrode B grounded, and a synchronization signal is sent to the μ-PIV setup. At $t = 150$ ms after reciving the synchronization signal, the μ-PIV setup fires the lasers and captures two images of the moving droplet with 5–20 ms of delay between them. The waiting time $t_w = 150$ ms is chosen so the droplet is moving at approximately midway between the two electrodes. At $t = 300$ ms, the actuation potential is switched onto electrode B for a duration of 300 ms, with electrode A grounded, to move the droplet back to electrode B. Starting from $t = 600$ ms, both electrodes are grounded for 1400 ms before the next cycle of movement/image capture is initiated. Sixty sets of image pairs are captured in this manner. A sufficient time between the image pair must be chosen to resolve the lowest flow speed in the center of the drop. This indirectly influences the spatial resolution of the experiment, since maximum particle displacement must be sufficiently smaller than the size of the interrogation region used by the μ-PIV software.[23] We analyze the image pairs using an interrogation region of 96 pixels × 96 pixels, which yields 2D velocity data at 32 μm × 32 μm resolution. As shown in Table 1, we repeat the procedure on 7 planes of different heights, z, above the bottom substrate to obtain a stack of 2D velocity fields. The 2D velocity fields at different t_w are obtained for the height $z = 148$ μm.

Results and discussion

2D velocity field

The inset of Fig. 3a shows the droplet image captured by bright field microscopy with a 4× objective lens during the droplet movement near the waiting time. The free interface shows up

Table 1 The height above the substrate and the delay time of μ-PIV captures

height/μm	delay times/ms
52	150
100	150
148	40, 80, 150, 210, 240, 280
196	150
244	150
292	150
340	150

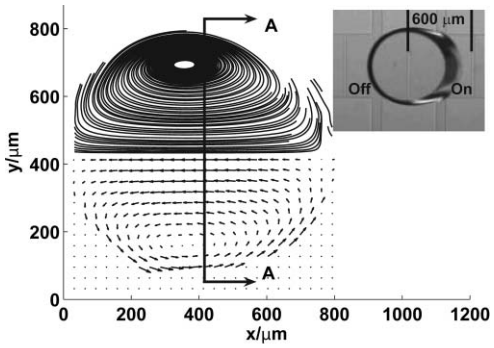

(a)

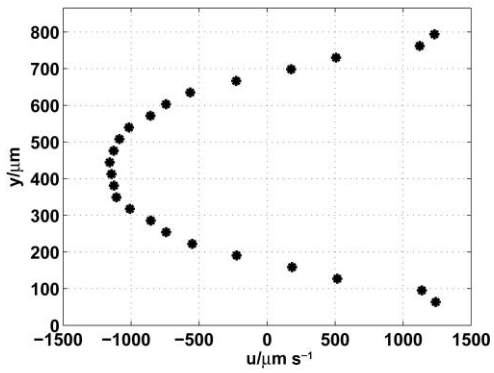

(b)

Fig. 3 (a) Two-dimensional velocity field at $z = 148$ μm (bottom half) and the streamlines (top half); (b) The axial velocity component, u, along the cross-section AA.

as a thick dark region surrounding the droplet because the curvature of the interface interferes with the light scattering. Therefore, we do not expect the μ-PIV to capture data in the region near the interface. Fig. 3a shows the 2D Lagrangian (*i.e.* viewed from a reference frame traveling with the droplet) velocity field computed from the PIV data and the streamlines at height $z = 148$ μm, where $z_{max} = 388$ μm. The speed of the droplet (*i.e.* the speed of the moving reference frame) is approximately 2 mm s^{-1}. Due to the lack of data near the interface, the streamline produced by the velocity field terminates there as expected. The 2D data clearly shows two internal circulations symmetric about the moving axis of the droplet, x. Fig. 3b shows a smooth variation of the axial velocity component along the cross-section of the 2D plane at $y = 426$ μm. The fluid flows forward along the free surface (*i.e.* liquid–air interface) of the droplet toward the nose and circulates backward near the center, a flow pattern similar to the one reported by Fowler *et al.*[18]

Flow circulations

We compute the 2D vorticity at each data point by finite difference,

$$\omega_{i,j} = \frac{\partial v_{i,j}}{\partial x} - \frac{\partial u_{i,j}}{\partial y} \tag{1}$$

Fig. 4 shows the contour plot of the vorticity generated by the two circulations at $t_w = 150$ ms. Significant vorticity for mixing processes are generated on the two sides of the droplet near the free surface. To get a better idea of the relationship between

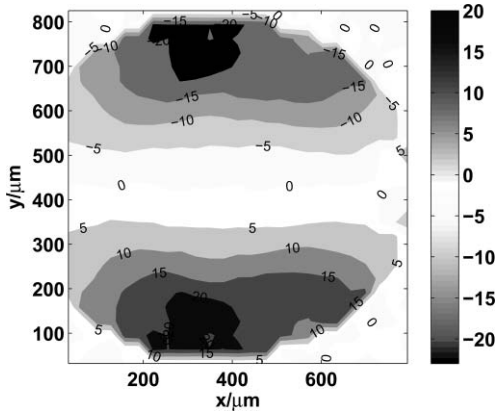

Fig. 4 Contour plot of the vorticity in the horizontal plane at $z = 148$ μm.

vorticity and the drop speed, we compute the mean velocity, at different t_w, on the horizontal plane $z = 148$ μm. Integration of the velocity over time gives us an estimate of the droplet displacement. For a droplet of 800 μm in disc diameter moving on electrodes of 600 μm in length, the nose of the droplet already extends approximately 200 μm into electrode A at the beginning of each capture sequence. Since the droplet stretches into an elliptical shape, we expect less than 400 μm of distance for the droplet to travel. Fig. 5a shows that the droplet moves steadily at a speed of about 2 mm s^{-1}, before slowing down as its nose approaches the far edge of electrode A. The steady movement is sustained for approximately 150 ms before the droplet slows down. To relate the circulation of vortices to the drop motion, we sum over the entire plane the absolute value of the vorticity,

$$\Gamma = \sum_{i=1}^{N}\sum_{j=1}^{M} |\omega_{i,j}|, \tag{2}$$

to estimate the strength of the circulation as shown in Fig. 5b. Comparing the velocity and the circulation strength shows a close correspondence between the two flow properties.

3D velocity field

For a 3D droplet, it is also important to understand how the fluid is circulating in the direction normal to the substrates. To obtain the velocity component normal to the substrates, w, we first compute the 2D divergence of the horizontal velocity measured on all 7 horizontal planes. Using the continuity equation, the normal gradient of w is

$$\frac{\partial w}{\partial z} = -\frac{\partial u}{\partial x} - \frac{\partial v}{\partial y}. \tag{3}$$

We do not have the data at the interface due to the interference from the curving air–liquid interface. Therefore, we restrict our attention to the bulk of the drop, where the data on all 7 planes are available. Since the aspect ratio of the drop, b/R, is close to 1, we expect the bulk flow to be 3D as well. We first interpolate a 7th order polynomial, $p(z)$, through the data of $\partial w/\partial z$ through all 7 planes,

$$p(z) = \sum_{n=1}^{7} c_n z^n, \tag{4}$$

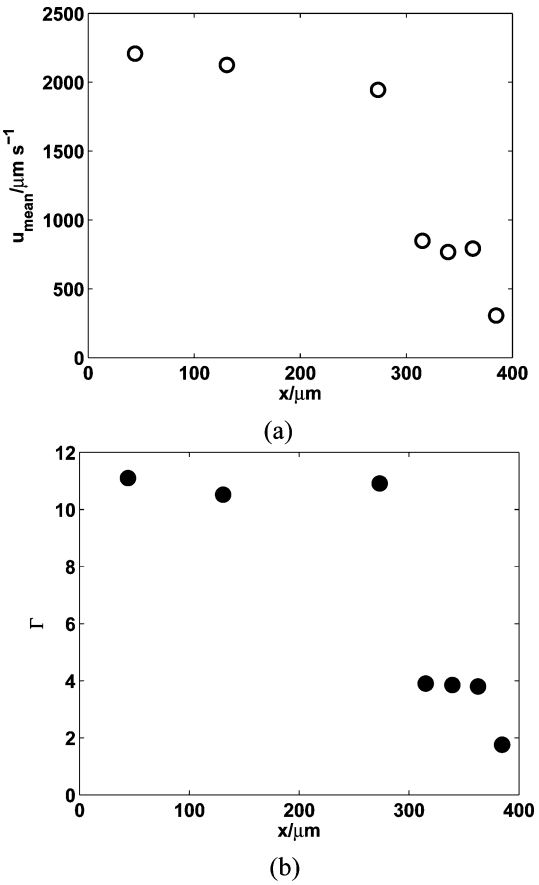

Fig. 5 (a) Mean velocity of the droplet at different locations; (b) Circulation strength of the flow at different center of masses locations.

with no-slip boundary condition at $z = 388$ μm. The no-slip boundary condition at $z = 0$ μm is automatically satisfied by the interpolation function we choose. Subsequently, integrating $p(z)$ gives us an estimate of the normal velocity component.

The 3D velocity field is shown in Fig. 6. Indeed, we observe 3D flows in the bulk of the droplet. The flow gains a significant normal velocity component as it approaches the drop interface. A strong downward flow due to the electrowetting from the bottom substrate is observed near the nose of the droplet. The fluid near the substrates circulates back into the droplet near the rear of the droplet. As shown in the vertical cross-sections (Fig. 7), the flow is asymmetric across the height of the droplet due to corresponding asymmetric actuation in the current EWOD devices. The significant recirculation in a thick drop suggests that the 3D flow stretches and folds the material interface across the height of the drop. This flow behavior reduces the striation length and enhances mixing, as analyzed by Handique *et al.*[24] for a slit-type channel. An extension of the analysis beyond the assumption of the fully developed parabolic flow profile is needed to analyze a thick 3D droplet.

To understand the net effect of the 3D flow between planes, we compute the overall displacements of the fluid by the 2-steps linear pattern in the μ-PIV experiment (Fig. 3) at $z = 148$ μm. Fig. 8 compares the instantaneous velocity field at $t_w = 150$ ms and the overall displacement field. The overall displacement field shown in Fig. 7b is symmetric about the moving axis, x. The field shows the fluid enter the horizontal plane near the nose

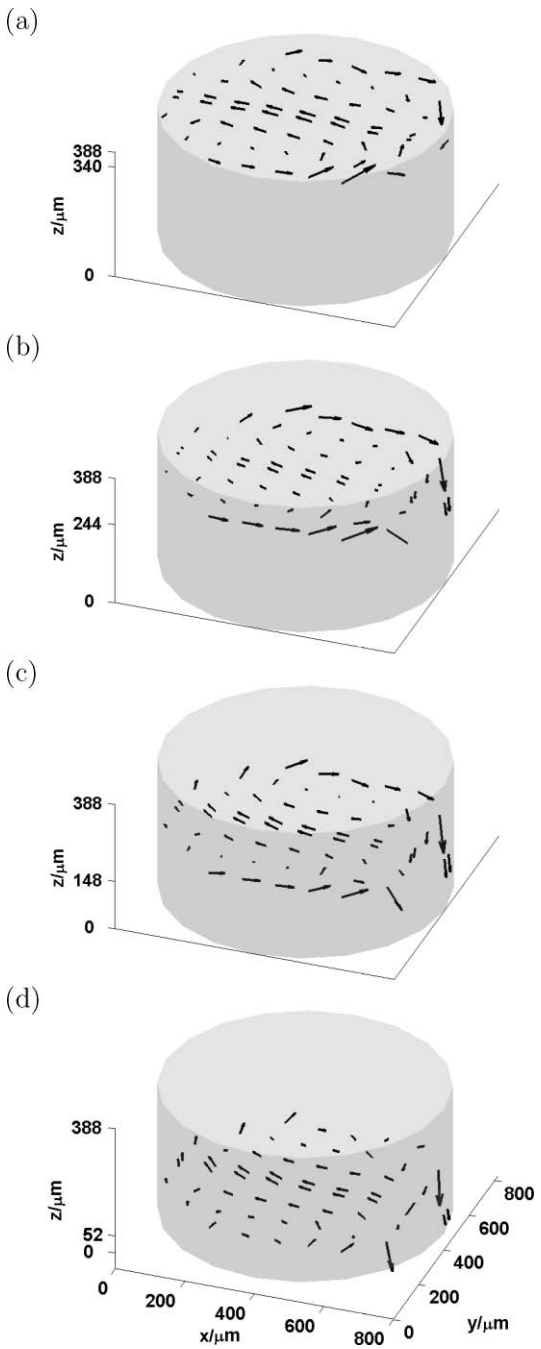

Fig. 6 The 3-dimensional velocity field at (a) $z = 340$ μm; (b) $z = 244$ μm; (c) $z = 148$ μm; (d) $z = 52$ μm.

($x = 800$ μm) and the tail ($x = 0$ μm) of the droplet. The flow converges toward two points near the front half of the droplet interface, where it exits in the z-direction out of the horizontal plane. Since the flow in the drop is unsteady, the direction of the displacement field does not necessarily follow the direction of the instantaneous velocity field. Integrating the displacements of tracer particles from random initial positions for 150 ms (Fig. 8a) shows that the Lagrangian velocity field of the forward droplet motion convects the tracer particles over a long distance (~100 μm). In contrast, the net displacements after one cycle of droplet actuation are much shorter (~10 μm) in different directions. This indicates the reverse droplet motion returns

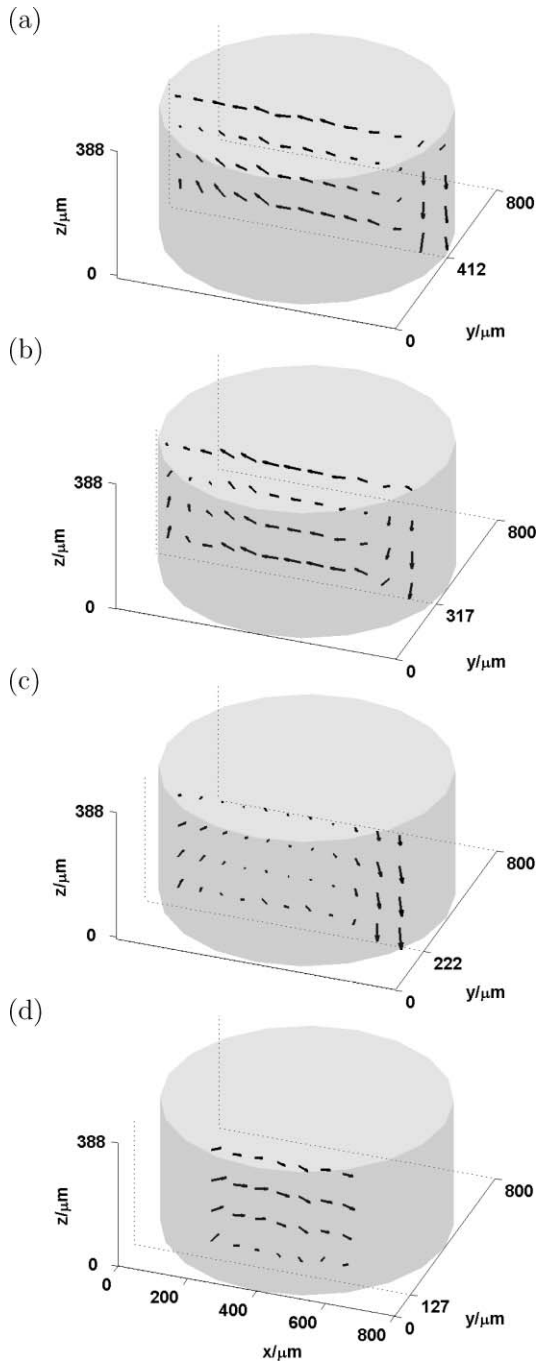

Fig. 7 Slices of x and z velocity components at (a) $y = 412$ μm; (b) $y = 317$ μm; (c) $y = 222$ μm; (d) $y = 127$ μm.

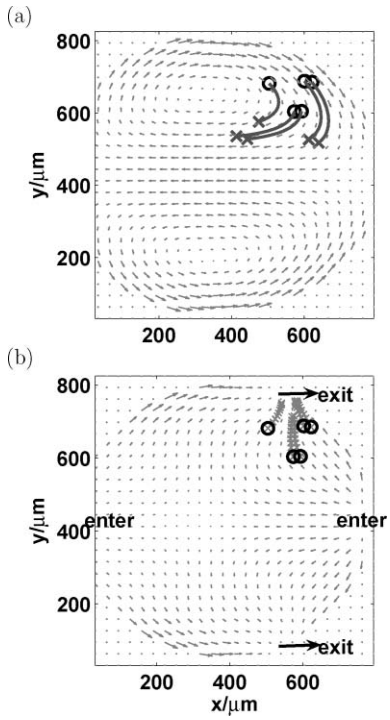

Fig. 8 The displacement of particles starting at random positions denoted by ○s. (a) The instantaneous velocity field at $t_w = 150$ ms and $z = 148$ μm. ×s denote the particle positions after 150 ms of convection by the instantaneous velocity field; (b) The overall displacement field at $z = 148$ μm by the forward-and-back droplet actuations. The flow enters the z plane near the nose and the tail of the droplet and exits out of the plane near the front half of the meniscus. ×s denote the ending positions of each cycle.

the particles back to near their initial positions, a reversible characteristic of a well-ordered laminar flow. As Fig. 8b shows, transporting the particles over a significant distance (>100 μm) requires 15 cycles of droplet actuations. Therefore, the forward-and-back motion is inefficient for droplet mixing, even if one considers dye with a higher diffusion coefficient.

Implication for mixing

The results above prompt us to revisit the mixing of droplets under EWOD-driven digital microfluidics: more specifically, the mixing strategy proposed by Fowler *et al.*[18] The dynamics can be modeled as a blinking vortex flow, a sequence of vortices turning on and off periodically at different locations,[25] making the flow in the drop a chaotic system.[26] An example of which is the square movement sequence proposed by Fowler *et al.*,[18] generating 4 pairs of vortices within the droplet.

We conducted a mixing experiment to quantify the mixing performance by different EWOD patterns using a water droplet and a dyed droplet of equal volume with low concentration (~1 mM) of Mordant Blue 9 (Acros Organics). We observed uniform diffusion of the dye across a static droplet after merging (Fig. 9a), indicating the absence of significant Marangoni convection. The standard deviation, σ, of the blue color pixel intensity is computed as an indication of mixing. We compare the mixing result between the square movement pattern and a 4-steps linear movement pattern composed of two forward steps and two backward steps. Fig. 9b shows the dye is well mixed by the square movement, while the linear movement pattern can not achieve the same level of mixing. The backward steps partially unmix the droplet, resulting in periodic peaks of σ, similar to the results described previously.

The understanding of the fluid dynamics allows us to relate the kinematics of the flow in the droplet with the device geometries. Khakhar *et al.*[27] showed that the mixing efficiency of the blinking vortex flow is dependent on the flow strength, μ. The flow

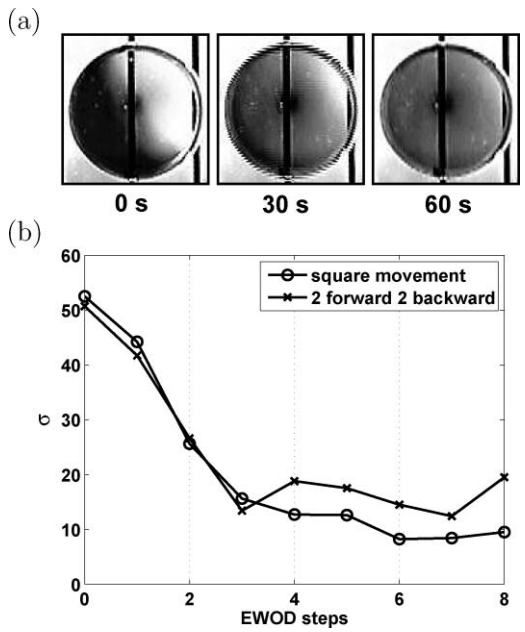

Fig. 9 (a) Diffusion of dye in a static drop; (b) The standard deviation of the dye's color intensity in drops mixed by different EWOD movement patterns.

strength is defined by

$$\mu = \frac{\Gamma T}{2\pi a}, \tag{5}$$

where Γ is the strength of the vortex, T is the period of the blinking vortices, and a is the distance between the vortices. They showed numerically that optimal mixing efficiency is achieved when $\mu = 0.8$. In the context of EWOD movements, the vortex strength is related to the mean speed of the droplet, U, which is related to the actuation voltage.[7] The period of the blinking vortices is also related to the speed of the droplet by L/U, where L is the length of the electrodes. The distance between the vortices is related to the drop diameter. All three physical parameters are controllable by the actuation voltage, the device geometry, and the drop size. Given a set of geometric parameters, such as drop sizes and the movement patterns, we can further improve the mixing efficiency by tuning the actuation period, a kinematic parameter, to achieve the optimal flow strength.

Conclusions

We characterized the internal flow of a thick droplet actuated by EWOD in a parallel-plate configuration using the μ-PIV technique. Our 2D data showed two symmetric circulations within the moving droplet. The reconstruction of the 3D velocity field showed that the flow in a 3D droplet deviates from the parabolic flow profile used in current flow simulations. Significant recirculation was observed near the droplet interface, which was neglected by the 2D reduction of the Navier–Stokes equation. For the specific application of mixing by EWOD, a simple forward-and-back motion was inefficient because the flow was under a low Reynolds number and somewhat reversible. We confirmed that an irreversible pattern that breaks the symmetry of the two horizontal circulations enhances mixing. In addition, the fundamental insights of the fluid dynamics that relate the geometry to the kinematics enable us to propose an actuation strategy to further improve mixing performance. Therefore, it is important to address the challenges of modeling and simulating a constrained 3D droplet with a free air–liquid interface in order to provide analytical tools for the field.

Acknowledgements

We thank Professor Pirouz Kavehpour for valuable discussions on PIV data analysis. This work is funded by ONR grant N000140710431, NSF grant ACI-0321917, NSF grant NIRT CTS-040444, NASA through Institute for Cell Mimetic for Space Exploration (CMISE), and NIH through Pacific Southwest RCE (grant AI065359).

Notes and references

1 M. G. Pollack, R. B. Fair and A. D. Shenderov, *Appl. Phys. Lett.*, 2000, **77**, 1725–1726.
2 J. Lee, H. Moon, J. Fowler, T. Schoellhammer and C.-J. Kim, *Sens. Actuators, A*, 2002, **A95**, 259–268.
3 S.-K. Cho, H. Moon and C.-J. Kim, *J. Microelectromech. Syst.*, 2003, **12**, 70–80.
4 F. Mugele and J. C. Baret, *J. Phys. Condens. Matter*, 2005, **17**, R705–R774.
5 R. B. Fair, *Microfluid. Nanofluid.*, 2007, **3**, 245–281.
6 H. Moon, and C.-J. Kim, in *Microfluidic Technologies for Miniaturized Analysis Systems*, ed. S. Hardt, and F. Schonfeld, Springer, New York, London, 2007, ch. 5, pp. 203–236.
7 H.-W. Lu, K. Glasner, A. L. Bertozzi and C.-J. Kim, *J. Fluid Mech.*, 2007, **590**, 411–435.
8 S. W. Walker and B. Shapiro, *J. Microelectromech. Syst.*, 2006, **15**, 986–1000.
9 D. J. Acherson, in *Elementary Fluid Dynamics*, Clarendon Press, Oxford, 1990.
10 F. Bottausci, C. Cardonne, I. Mezic I. and C. D. Meinhart, *Lab Chip*, 2007, **7**, 396–398.
11 Y.-K. Lee, C. Shih, P. Tabeling and C.-M. Ho, *J. Fluid Mech.*, 2007, **575**, 425–448.
12 J. C. Rife, M. I. Bell, J. S. Horwitz, M. M. Kabler, R. C. Y. Auyeung and W.-J. Kim, *Sens. Actuators, A*, 2000, **86**, 135–140.
13 R.-H. Liu, M. A. Stremler, K. V. Sharp, K. G. Olsen, J. G. Santiago, R. J. Adrian, H. Aref and D. J. Beebe, *J. Microelectromech. Syst.*, 2000, **9**, 190–197.
14 A. D. Stroock, S. K. W. Dertinger, A. Ajdari, I. Mezic, H. A. Stone and G. M. Whitesides, *Science*, 2002, **295**, 647–651.
15 H. Song, J.-D. Tice and R. F. Ismagilov, *Angew. Chem., Int. Ed.*, 2003, **42**, 768–772.
16 F. Mugele, J. C. Baret and D. Steinhauser, *Appl. Phys. Lett.*, 2006, **88**, 204106-1-3.
17 J. Aizenberg, T. Krupenkin and P. Kolodner, *Mater. Res. Soc. Symp. Proc.*, 2006, **915**, 103–111.
18 J. Fowler, H. Moon, C.-J. Kim, *Proceedings of IEEE MEMS Conference*, Las Vegas, 2002, pp. 97–100.
19 P. Paik, V. K. Pamula and R. B. Fair, *Lab Chip*, 2003, **4**, 253–259.
20 J. G. Santiago, S. T. Wereley, C. D. Meinhart, D. J. Beebe and R. J. Adrian, *Exp. Fluids*, 1998, **25**, 316–319.
21 C. D. Meinhart, S. T. Wereley and J. G. Santiago, *Exp. Fluids*, 1999, **27**, 414–419.
22 S.-K. Fan, C. Hashi, C.-J. Kim, *Proceedings of IEEE MEMS Conference*, Kyoto, 2003, pp. 694–697.
23 S. T. Wereley, L. Gui and C. D. Meinhart, *AIAA J.*, 2001, **40**, 1047–1055.
24 H. Handique and M. A. Burns, *J. Micromech. Microeng.*, 2000, **11**, 548–554.
25 H. Aref, *J. Fluid Mech.*, 1984, **143**, 1–21.
26 J. M. Ottino, *The Kinematics of Mixing: Stretching, Chaos, and Transport*, Cambridge University Press, Cambridge, 1989.
27 D. V. Khakhar, H. Rising and J. M. Ottino, *J. Fluid Mech.*, 1986, **172**, 419–451.